

Instability of a boundary layer flow on a vertical wall in a stably stratified fluid

Jun Chen¹, Yang Bai^{1,2} and Stéphane Le Dizès^{1,†}

¹Aix Marseille Université, CNRS, Centrale Marseille, IRPHE, UMR 7342, Marseille, F-13013, France

²Université du Havre, CNRS, LOMC, UMR 6294, Le Havre, F-76058, France

(Received 1 June 2015; revised 12 January 2016; accepted 14 March 2016)

The stability of a horizontal boundary layer flow on a vertical wall in a viscous stably stratified fluid is considered in this work. A temporal stability analysis is performed for a tanh velocity profile as a function of the Reynolds number $Re = UL/\nu$ and the Froude number $F = U/(LN)$ where U is the main stream velocity, L the boundary layer thickness, N the buoyancy frequency and ν the kinematic viscosity. The diffusion of density is neglected. The boundary layer flow is found to be unstable with respect to two instabilities. The first one is the classical viscous instability which gives rise to Tollmien–Schlichting (TS) waves. We demonstrate that, even in the presence of stratification, the most unstable TS wave remains two-dimensional and therefore independent of the Froude number. The other instability is three-dimensional, inviscid in nature and associated with the stratification. It corresponds to the so-called radiative instability. We show that this instability appears first for $Re \geq Re_c^{(r)} \approx 1995$ for a Froude number close to 1.5 whereas the viscous instability develops for $Re \geq Re_c^{(v)} \approx 3980$. For large Reynolds numbers, the radiative instability is also shown to exhibit a much larger growth rate than the viscous instability in a large Froude number interval. We argue that this instability could develop in experimental facilities as well as in geophysical situations encountered in ocean and atmosphere.

Key words: boundary layer stability, stratified flows

1. Introduction

Boundary layers are ubiquitous in any flow close to boundaries. They are known to be unstable with respect to viscous instabilities for Reynolds numbers above a few thousands. In the presence of a stable stratification, such a flow on a vertical wall is shown to be unstable with respect to a stronger instability associated with the emission of internal gravity waves. The goal of the present article is to analyse the competition between both instabilities for a simple model of boundary layer flow as a function of viscosity and stratification strength.

The stability of boundary layer flows is a subject almost as old as fluid mechanics and is covered by several textbooks (e.g. Betchov & Criminale 1967). In particular, it is well established that an inflection-free boundary layer profile is unstable with respect to a two-dimensional (2-D) viscous instability that gives rise to the so-called Tollmien–Schlichting (TS) waves.

† Email address for correspondence: ledizes@irphe.univ-mrs.fr

The effect of a stable stratification has been mainly studied in the context of atmospheric flows on flat horizontal surfaces (see Mahrt 2014, for a review). However, in this context, the velocity profile usually exhibits an inflectional point which makes it unstable with respect to the Kelvin–Helmholz instability. This instability is modified by stratification as shown in Howard (1961), Miles (1961), Churilov (2005, 2008), Candelier, Le Dizès & Millet (2011). The effect of stratification on TS waves is less well understood. It was studied experimentally in Ohya & Uchida (2003). Wu & Zhang (2008a) also demonstrated that it could be destabilizing. On a vertical wall, the 2-D TS waves are not expected to be affected by stratification. But as Squire theorem is not applicable in the presence of stratification, more unstable three-dimensional (3-D) TS waves could *a priori* exist.

The inclination of shear with respect to the direction of stratification is also known to be a source of instability. Candelier, Le Dizès & Millet (2012) showed that an inflection-free boundary layer profile becomes unstable with respect to an inviscid ‘radiative instability’ as soon as there is an angle between the directions of shear and stratification, the instability being the strongest for an angle of $\pi/2$, that is for a vertical wall. This instability, which results from the coupling between shear and internal waves, has been obtained in other contexts: shallow water flows (Satomura 1981; Balmforth 1999; Riedinger & Gilbert 2014), compressible flows (Mack 1990; Parras & Le Dizès 2010) and rotating flows (Riedinger, Le Dizès & Meunier 2010, 2011). It has often been associated with a phenomenon of resonant over reflection (McIntyre & Weissman 1978; Grimshaw 1979; Lindzen & Barker 1985), negative energy waves (Kopev & Leontev 1983) or spontaneous wave emission (Plougonven & Zeitlin 2002; Le Dizès & Billant 2009). In the present work, we shall analyse the effect of viscosity on the radiative instability of a boundary layer.

The paper is organized as follows. In §2, we present the framework, the perturbation equations and the numerical method. In §3.1, we first analyse the effect of stratification on the viscous instability and then in §3.2 study the radiative instability in the presence of viscosity. In §3.3, we provide a summary of the stability results. The last section (§4) is a brief discussion in the context of applications.

2. Mathematical formulation

2.1. Base flow and perturbation equations

We consider a horizontally directed flow adjacent to a vertical wall in a non-rotating, incompressible viscous stably stratified fluid, as sketched in figure 1. The stratification is assumed to be uniform with a constant buoyancy frequency

$$N = \sqrt{\frac{g}{\rho_0} \frac{\partial \bar{\rho}}{\partial y}}, \quad (2.1)$$

where g is gravity, ρ_0 is a characteristic value of the mean density $\bar{\rho}$. As commonly done in the context of boundary layer stability, we apply a local parallel-flow assumption and assume that the base flow velocity field is given by the tanh profile

$$\bar{\mathbf{u}} = U_0(z) \mathbf{e}_x = U \tanh\left(\frac{z}{L}\right) \mathbf{e}_x, \quad (2.2)$$

where \mathbf{e}_x is the unit vector in the streamwise direction x . The local characteristic velocity U and boundary layer thickness L are used to non-dimensionalize all the variables. The local parallel-flow assumption gives a constraint on the streamwise perturbation wavelength which should be much smaller than the viscous evolution length. We shall discuss this constraint in §4.

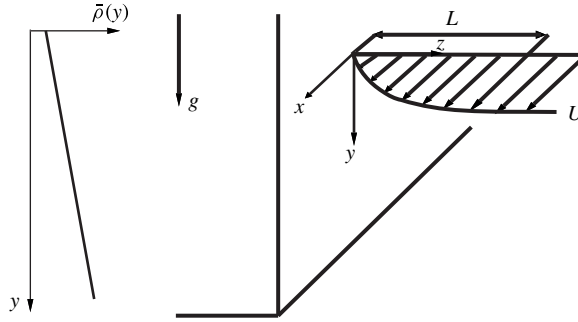


FIGURE 1. Sketch of the flow geometry.

The choice of a tanh profile (instead of a Blasius profile) has been made for numerical convenience. Both the viscous and the radiative instabilities that we discuss here are expected to be weakly sensitive to the details of the profile (as long as it remains non-inflectional). In the very large Reynolds number limit, it is indeed known that the characteristics of these instabilities only depend on the velocity derivatives at the boundary (see Drazin & Reid (1981) for the viscous instability and Candelier *et al.* (2012) for the radiative instability).

The base flow is defined by three parameters:

$$Re = \frac{UL}{\nu} \quad \text{the Reynolds number,} \quad (2.3a)$$

$$Sc = \frac{\nu}{D} \quad \text{the Schmidt number,} \quad (2.3b)$$

$$F = \frac{U}{NL} \quad \text{the Froude number,} \quad (2.3c)$$

where ν and D are the kinematic viscosity and the mass diffusivity of the fluid.

In the present study, the Froude and Reynolds numbers are varied in the intervals

$$100 < Re < 10^7, \quad 0.01 < F < 20. \quad (2.4a,b)$$

We neglect the diffusion of mass and set $Sc = \infty$. This hypothesis is valid for salty water, for which Sc is around 700.

The goal of the present study is to perform a linear temporal stability analysis of the base flow (2.2). Perturbations are then searched in the form of normal modes

$$(u', v', w', p', \rho') = (u, v, w, p, F^2 \bar{\rho} b) e^{ik_x x + ik_y y - i\omega t}, \quad (2.5)$$

where k_x and k_y are real wavenumbers and ω the complex eigenfrequency. The velocity, pressure and buoyancy amplitudes (u, v, w, p, b) satisfy the following equations obtained by linearizing the Navier–Stokes and density equations under the Boussinesq approximation

$$-i\Phi u + \frac{dU_0}{dz} w = -ik_x p + \frac{1}{Re} \Delta_z u, \quad (2.6a)$$

$$-i\Phi v = -ik_y p + b + \frac{1}{Re} \Delta_z v, \quad (2.6b)$$

$$-i\Phi w = -\frac{dp}{dz} + \frac{1}{Re}\Delta_z w, \tag{2.6c}$$

$$-i\Phi b + \frac{1}{F^2}v = 0, \tag{2.6d}$$

$$ik_x u + ik_y v + \frac{dw}{dz} = 0, \tag{2.6e}$$

where

$$\Phi = \omega - k_x U_0(z), \tag{2.7a}$$

$$\Delta_z = \frac{d^2}{dz^2} - k_x^2 - k_y^2. \tag{2.7b}$$

The no-slip boundary condition gives $u(0) = v(0) = w(0) = 0$. Far away from the boundary, we apply a condition of radiation which prescribes that the energy should propagate outward.

2.2. Numerical method

The system (2.6a–e) is discretized using a pseudo-spectral method on the collocation points of Laguerre polynomials. These polynomials are well adapted to semi-infinite domain $[0, +\infty[$. This method has already been used in Riedinger *et al.* (2010) and Candelier *et al.* (2012). The system of equations is then transformed into a generalized eigenvalue problem $A\mathbf{f} = \omega\mathbf{B}\mathbf{f}$ for $\mathbf{f} = [u, v, w, p, b]$, which is solved using subroutines of Matlab©.

The eigenfunctions obtained by this method automatically vanish at infinity. As already explained by Riedinger *et al.* (2010), this is not an adequate behaviour for all the physical perturbations.

By considering (2.6) for large z , it is easy to show that all solutions are a sum of exponentials $e^{i\beta z}$ with $\Lambda = k_x^2 + k_y^2 + \beta^2$ satisfying

$$(\Lambda - i(\omega - k_x)Re)[i(\Lambda - k_y^2)Re - \Lambda F^2(\omega - k_x)(\Lambda - i(\omega - k_x)Re)] = 0. \tag{2.8}$$

The condition of radiation prescribes that the solution should expend at infinity on three exponentials among the six possible (only the exponentials corresponding to waves propagating energy outward are kept). When $\text{Im}(\omega) > 0$, this condition of radiation is equivalent to discarding the growing exponentials and keeping the decreasing exponentials. It is therefore equivalent to the vanishing of the solution at infinity. This implies that all unstable modes can *a priori* be captured by the spectral code. When $\text{Im}(\omega) = 0$ or $\text{Im}(\omega) < 0$, the conditions of radiation and of vanishing do not necessarily match. There are large regions of the complex ω plane where these two conditions are not equivalent. In these regions, the modes obtained by the spectral code are therefore ‘unphysical’. The boundaries of these regions correspond to curves in the ω plane where one of the wavenumbers β satisfying (2.8) becomes real. These curves are the so-called continuous spectrum. An illustration showing the numerical spectrum and the continuous spectrum is displayed in figure 2(a) for a typical example. In this figure, we have indicated by a dashed rectangle the region of the ω plane where the interesting eigenvalues corresponding to the radiative instability are expected. This region is very close to the continuous spectrum, which means that the eigenfunctions decay slowly at infinity. As explained in Riedinger *et al.* (2010), the

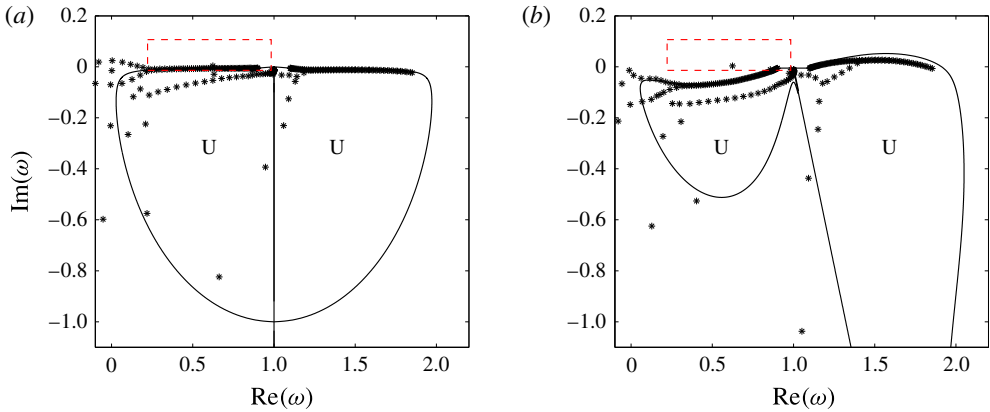


FIGURE 2. (Colour online) Continuous spectrum (solid lines) and numerical eigenvalues (stars) for $N = 100$ and the parameters $Re = 10^4$, $F = 1$, $k_x = 1$, $k_y = 10$. The ‘unphysical’ domain is indicated by the letter ‘U’. (a) Integration on the real axis ($\alpha = 0$); (b) integration on a complex path $z' = ze^{-i\alpha}$ with $\alpha = \pi/20$. The eigenvalue domain of interest is indicated by the dashed rectangle.

exponentially decreasing behaviour of the solution can be improved by introducing a complex mapping $z = z'e^{i\alpha}$ where α is a fixed positive angle. Such a mapping modifies an oscillating behaviour on the z variable, say $e^{i\beta z}$ with $\beta > 0$ to an exponentially decreasing behaviour $e^{i\beta \cos \alpha z'} e^{-\beta \sin \alpha z'}$ on the z' variable. The mapping thus modifies the spectrum and the continuous spectrum as shown in figure 2(b). The unstable mode in the dashed rectangle is now further away from the continuous spectrum curve. Being localized nearer to the origin, this mode is more easily resolved by the pseudo-spectral code. Neutral eigenvalues as well as weakly damped eigenvalues can also be captured by this method.

As soon as an eigenvalue is obtained, its robustness is tested by varying the angle α and the number N of polynomials. We have typically used $\alpha = \pi/20$ and $N = 100$.

3. Temporal stability results

3.1. Boundary layer instability (Tollmien–Schlichting waves)

Considering a boundary layer flow, the viscous instability associated with TS waves is expected to be active. Without stratification ($F = \infty$), the viscous instability of a boundary layer profile has been known for a long time (see for instance Betchov & Criminale 1967). In that case, Squire’s theorem is applicable: the most unstable mode among all the possible wavenumbers k_x and k_y is obtained for $k_y = 0$. Being 2-D without variation in the stratification direction y , this mode is also expected to exist in the presence of stratification, as the equations for the transverse velocity v and the buoyancy b are decoupled from the other velocity components and the pressure. However, there is no Squire theorem which guarantees that this 2-D mode remains the most unstable in the presence of stratification.

The effect of the Froude number on the growth rate curve in the (k_x, k_y) plane is illustrated in figure 3. In these plots, we do see that for a given Reynolds number, the instability domain associated with the viscous instability grows as the stratification increases while the largest growth rate in this (k_x, k_y) domain is still reached for $k_y = 0$. We have tried other values of the Reynolds number, and have always found that the

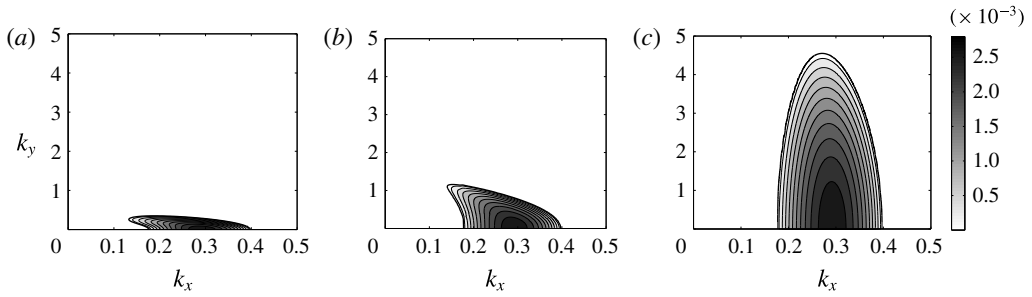


FIGURE 3. Growth rate contours of the viscous instability in the (k_x, k_y) plane for $Re = 10^4$ and different Froude numbers. (a) $F = \infty$ (unstratified case); (b) $F = 1$; (c) $F = 0.1$. Contours are every 0.00025 from 0 to 0.0028.

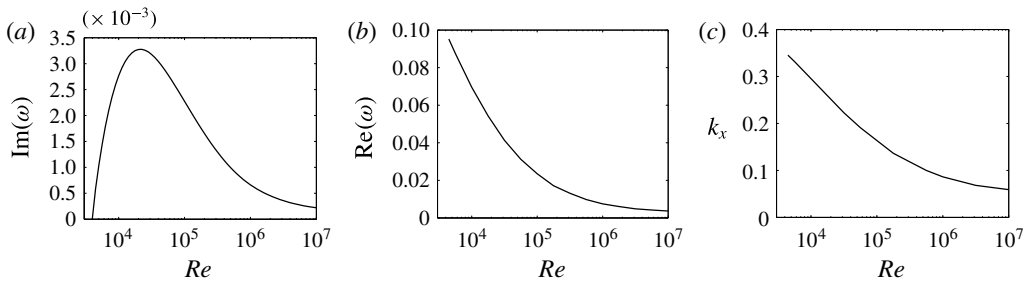


FIGURE 4. Characteristics of the most unstable TS wave as a function of Re . (a) Growth rate $\text{Im}(\omega)$; (b) oscillation frequency $\text{Re}(\omega)$; (c) wavenumber k_x .

most unstable TS wave, among all the possible wavenumbers k_x and k_y , remains 2-D whatever the Froude number. Since this mode does not depend on F , it means that its characteristics are not affected by the stratification. The characteristics of the most unstable TS wave are therefore independent of the stratification. They are shown in figure 4 as a function of the Reynolds number. The critical Reynolds number is found to be $Re_c^{(v)} \approx 3981$ for which the critical TS wave has the characteristics: $k_x = 0.35$, $\omega = 0.1$. The growth rate decreases for large Reynolds numbers. It reaches its maximum at the most dangerous Reynolds number $Re_m^{(v)} \approx 22390$ for the most dangerous mode of characteristics $k_x = 0.13$, $\omega = 0.016 + 0.0033i$.

The eigenfunctions of the critical and most dangerous TS waves are presented in figure 5. Note that the eigenfunctions of both modes are very similar. The only noticeable difference is the stronger localization of the critical mode close to the boundary. This can be related to the streamwise wavenumber difference and the behaviour in $e^{-k_x z}$ of the eigenfunctions far from the boundary.

The evidence that Squire's theorem is not applicable in the presence of stratification is given in figure 6 which is an extension in a larger (k_x, k_y) domain of the growth rate contours. We clearly see the presence of 3-D modes which are more unstable than all the 2-D modes. These 3-D unstable modes are associated with another instability, the so-called radiative instability, analysed in the next section.

3.2. Radiative instability

The radiative instability is inviscid in nature and results from the coupling between shear and internal gravity waves associated with the fluid stratification. The inviscid

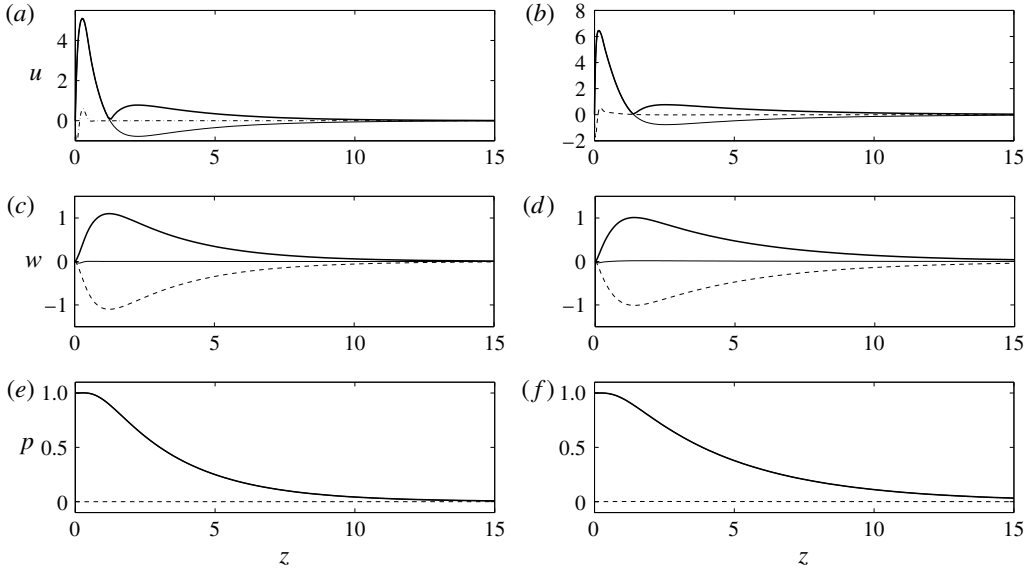


FIGURE 5. Eigenfunctions of the most unstable TS wave ((a,b) streamwise velocity u ; (c,d) normal velocity w ; (e,f) pressure p) for the critical Reynolds number $Re = Re_c^{(v)} \approx 3981$ (a,c,e) and the most dangerous Reynolds number $Re = Re_m^{(v)} \approx 22\,390$ (b,d,f). Thick solid lines, solid lines and dashed lines represent absolute value, real part and imaginary part, respectively.

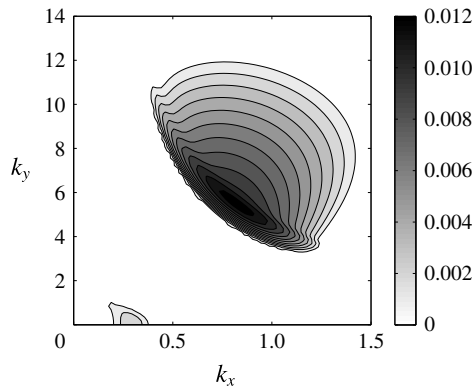


FIGURE 6. Growth rate contours in the (k_x, k_y) plane for $Re = 10^4$ and $F = 1$ (enlarged view of figure 3b). The two regions correspond to the viscous and radiative instability respectively. Contours are every 0.001 from 0.001 to 0.012.

characteristics of this instability have been obtained for the tanh boundary layer profile in Candelier *et al.* (2012).

In figure 7, we have plotted the growth rate of the (most unstable) radiative mode in the (k_x, k_y) plane for various Froude and Reynolds numbers. (Several unstable radiative modes may exist for a given set of parameters (k_x, k_y, Re, F) . We always keep the mode with the largest growth rate even if we do not systematically mention that it is the most unstable radiative mode). We clearly see that viscous effects reduce the

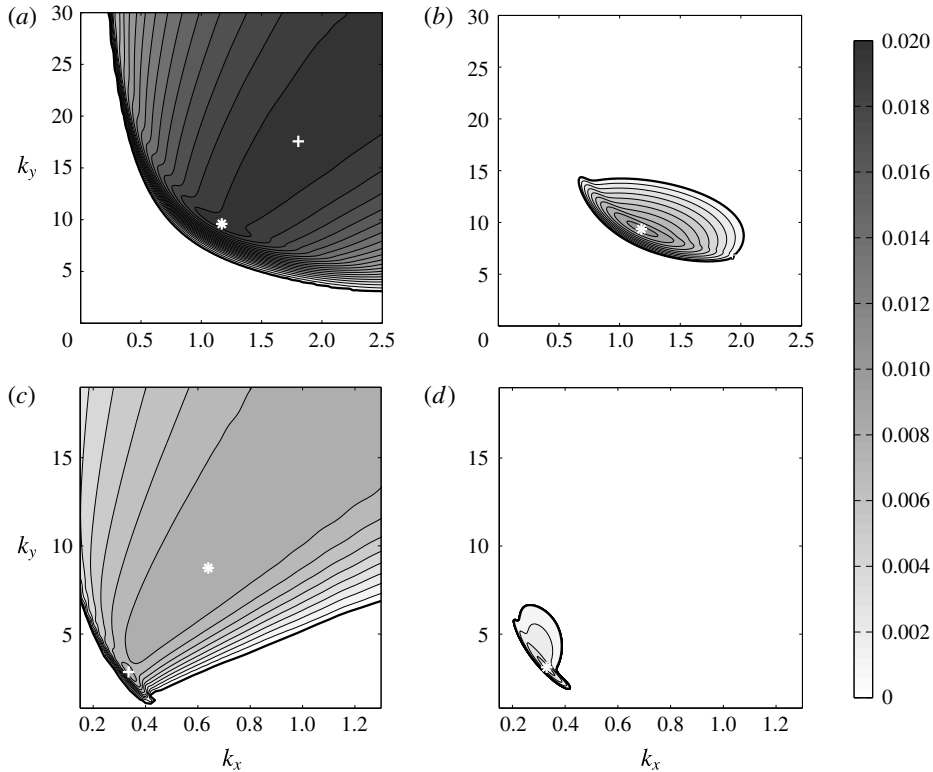


FIGURE 7. Growth rate contours of the radiative mode in the (k_x, k_y) plane for several sets of Froude and Reynolds numbers. (a) $Re = 10^7$, $F = 0.5$; (b) $Re = 10^4$, $F = 0.5$; (c) $Re = 10^7$, $F = 3$; (d) $Re = 10^4$, $F = 3$. White crosses indicate local maxima of the growth rate, the largest maximum being shown with an asterisk. Contours are every 0.001 from 0.001 to 0.02.

domain of instability. In the inviscid limit, the maximum growth rate is obtained for infinite k_x and k_y (Candelier *et al.* 2012). As soon as viscous effects are present, the maximum growth rate is reached for finite k_x and finite k_y . In figure 8, we have plotted the maximal value of the growth rate over all k_y as a function of k_x for various Reynolds numbers and $F = 0.5$ and 3. The viscous damping of higher wavenumbers is also clearly seen on these plots. It should be noticed that there are the two local peaks of the growth rate curve for $Re = 10^6$ and 10^7 . These peaks have also been indicated by symbols in figure 7(a,c). While the first peak remains almost fixed, the location of the second peak strongly varies with Reynolds number. This strong variation can be associated with the extremely broad character of this peak and the fact that it goes to infinity as $Re \rightarrow \infty$.

In figure 9, we have plotted the characteristics of the most unstable radiative mode (growth rate maximized over all the possible wavenumbers (k_x, k_y)) as a function of the Froude number for different Reynolds numbers. As expected, viscous results tend to inviscid results as Re increases. Note however that the convergence is slow, especially for small Froude numbers. This can be explained by the fact that even for $Re = 10^7$, the most unstable wavenumbers are still of order 1 (remember, they should go to infinity in the inviscid limit). For this Reynolds number, the most unstable

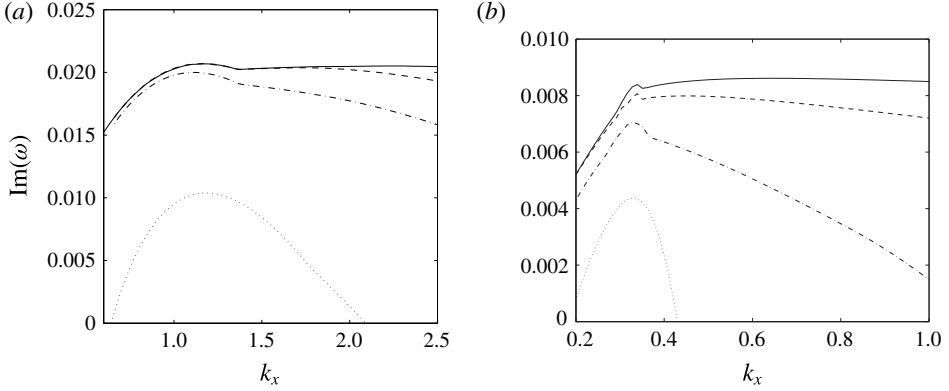


FIGURE 8. Maximum growth rate $\max_{k_y} [\text{Im}(\omega)]$ of the radiative modes versus k_x for $F = 0.5$ (a) and $F = 3$ (b). Solid line: $Re = 10^7$, dashed line: $Re = 10^6$, dash-dot line: $Re = 10^5$, dotted line: $Re = 10^4$.

wavenumbers correspond to the first peak of the growth rate curve in the (k_x, k_y) plane for all Froude numbers $F < 1$ (see figure 7a). It jumps to the second local peak of larger wavenumbers for higher Reynolds numbers, or for larger Froude numbers (see figure 7c). This change of modes as Froude or Reynolds number increases generates the jump observed in figure 9(c–f).

The results for the radiative instability are summarized in figure 10. In this figure, we have displayed the characteristics of the most unstable radiative mode as a function of both parameters Re and F . Only the growth rate contours are expected to be smoothed. The frequency, wavenumbers and phase velocities exhibit discontinuities which are associated with the local growth rate peak jumps discussed above. We have observed a single jump which is indicated by the dashed line in figure 10(b–d).

The critical Reynolds number for the radiative instability is found to be $Re_c^{(r)} \approx 1995$ and is reached for $F_c^{(r)} \approx 1.51$. The characteristics of the critical radiative mode are $k_x \approx 0.615$, $k_y \approx 4.236$, $\omega \approx 0.535$. As expected, the Froude number instability range increases with the Reynolds number, but the most unstable growth rates are obtained for strongly stratified configurations for which F is smaller than 1. In figure 10(a), the white dotted line gives the Froude number which maximizes the radiative instability for a prescribed Reynolds number.

The behaviour of constant growth rate curves for small Froude and large Reynolds numbers can be obtained by adding the viscous corrections to the non-viscous estimate. In this limit, Candelier *et al.* (2012) have indeed shown that the most unstable inviscid mode was obtained for $k_y/k_x \sim 4.9/F$. This means that for small F , k_y is much larger than k_x as well as the wavenumber based on the characteristic scale in the normal direction (z) which varies as k_x . The viscous damping of the mode is then expected to be just $-k_y^2/Re$. If we assume that k_x is approximately constant, this gives a viscous growth rate which is constant on the line $Re F^2 = \text{Cst}$, as approximately observed in figure 10(a).

The eigenfunctions of the distinguished radiative modes marked by symbols in figure 7 are shown in figures 11 and 12. Figure 11(a,b) shows the pressure eigenfunction of the most unstable mode for a weakly stratified configuration ($F = 3$) at $Re = 10^4$ and 10^7 . The pressure eigenfunction for $Re = 10^7$ strongly resembles the inviscid eigenfunction obtained by Candelier *et al.* (2012) for large Froude numbers

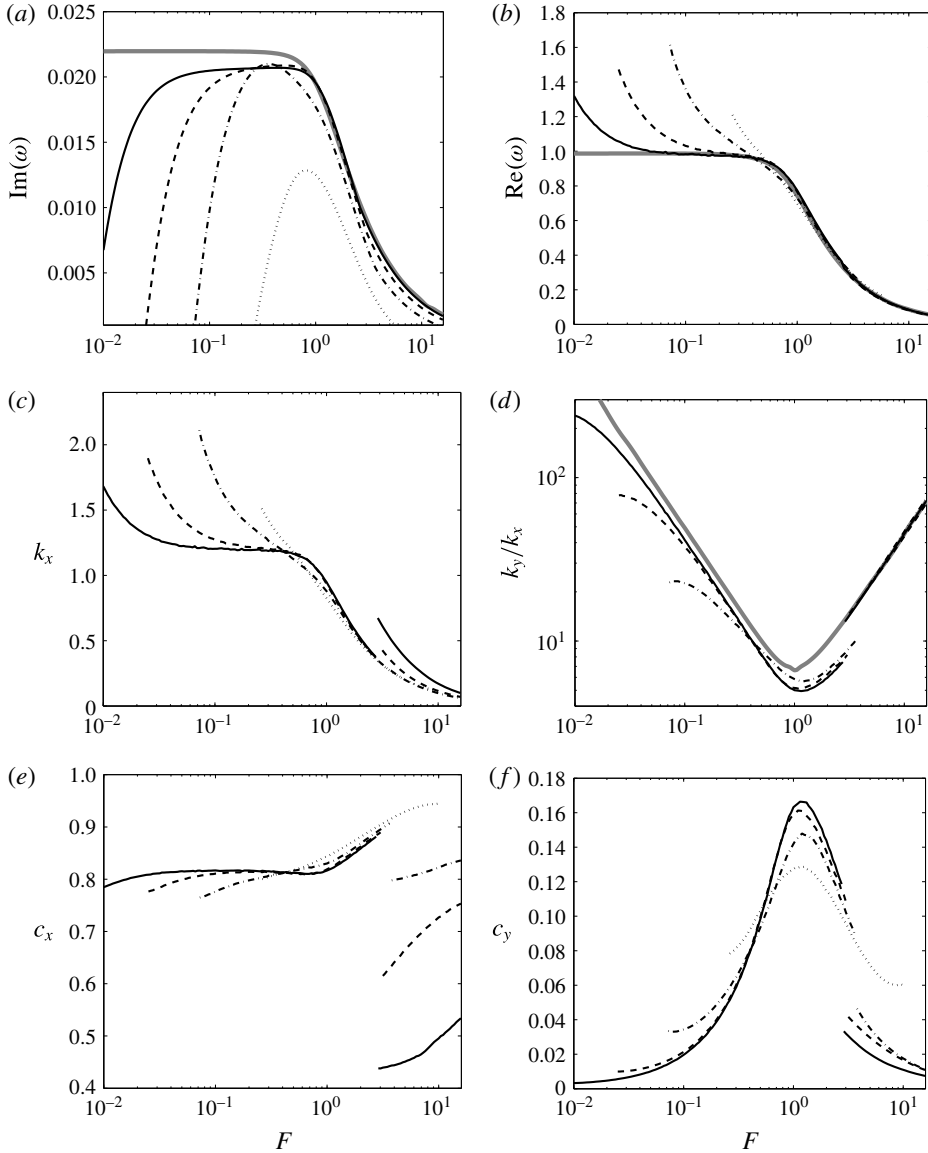


FIGURE 9. Characteristics of the most unstable radiative mode (obtained by maximizing the growth rate over all k_x and k_y) as a function of the Froude number F for different Reynolds numbers. $Re = 10^4$ (dotted line), 10^5 (dash-dot line), 10^6 (dashed line), 10^7 (solid line), ∞ (thick grey line). (a) Growth rate $\text{Im}(\omega)$; (b) oscillation frequency $\text{Re}(\omega)$; (c) streamwise wavenumber k_x ; (d) wavenumber ratio k_y/k_x ; (e) phase velocity $\text{Re}(\omega)/k_x$ along x ; (f) phase velocity $\text{Re}(\omega)/k_y$ along y .

and large wavenumbers. For smaller Reynolds numbers, the eigenfunction is by contrast different. These differences are not due to a change of instability mode. The modes are on the same instability branch but they are associated with two different local peaks of the growth rate contours in the (k_x, k_y) plane. For $Re = 10^4$, the most unstable mode corresponds to the first peak, while it is the second peak for $Re = 10^7$

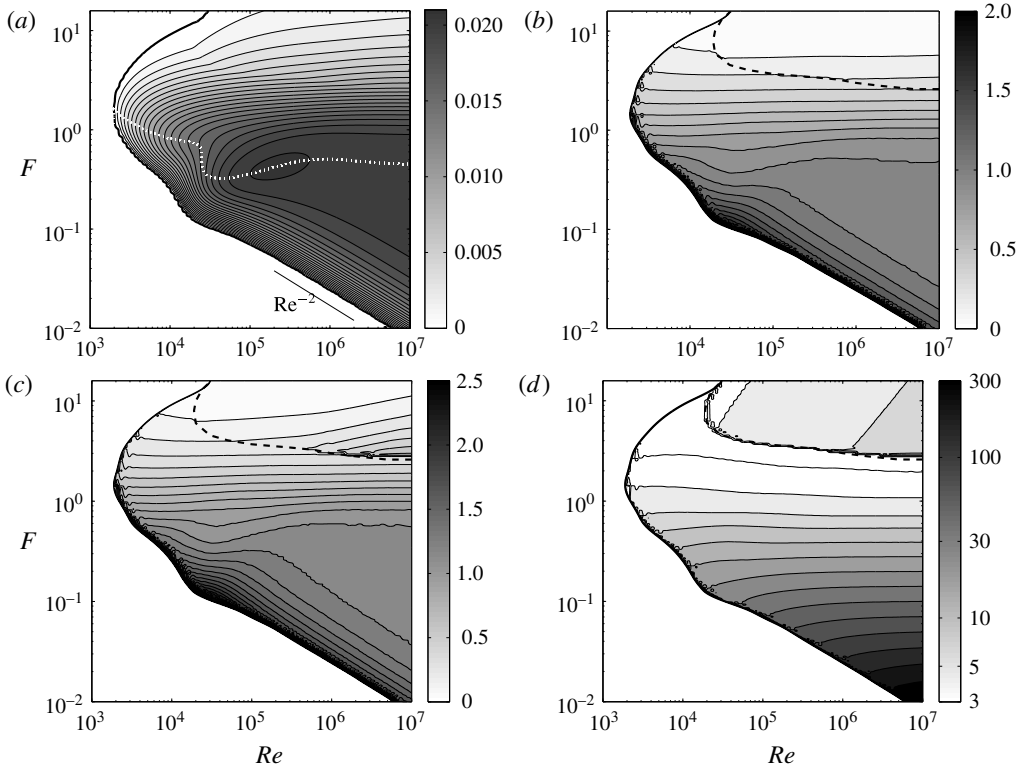


FIGURE 10. Characteristics of the most unstable radiative mode (obtained by maximizing the growth rate over all k_x and k_y) in the (Re, F) plane. (a) Growth rate $(\text{Im}(\omega))$ contours; (b) oscillation frequency $(\text{Re}(\omega))$ contours (in the unstable region); (c) streamwise wavenumber (k_x) contours; (d) transverse wavenumber (k_y) contours. The black dashed line indicates a discontinuity. The white dotted line in (a) gives the value of F which maximizes the growth rate for a fixed Re .

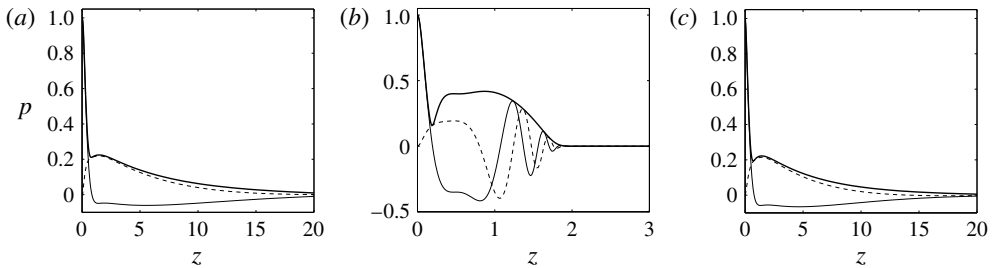


FIGURE 11. Pressure eigenfunction of distinguished radiative modes for $F = 3$ and two Reynolds numbers (corresponding to the symbols of figure 7*c,d*). (a) Most unstable mode for $Re = 10^4$: $k_x = 0.33$, $k_y = 3.13$, $\omega = 0.2971 + 0.0043i$; (b) most unstable mode for $Re = 10^7$: $k_x = 0.64$, $k_y = 8.75$, $\omega = 0.2817 + 0.0086i$; (c) less unstable mode corresponding to the first local peak of the growth rate curves for $Re = 10^7$: $k_x = 0.34$, $k_y = 2.75$, $\omega = 0.3023 + 0.0084i$. Thick solid lines, solid lines and dashed lines represent absolute value, real part and imaginary part, respectively.

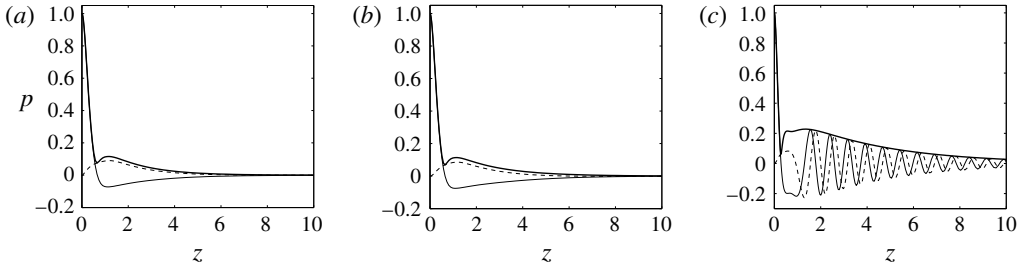


FIGURE 12. Pressure eigenfunction of distinguished radiative modes for $F=0.5$ and two Reynolds numbers (corresponding to the symbols of figure 7*a,b*). (a) Most unstable mode for $Re=10^4$: $k_x=1.18$, $k_y=9.34$, $\omega=0.964+0.011i$; (b) most unstable mode for $Re=10^7$: $k_x=1.17$, $k_y=9.58$, $\omega=0.9499+0.0209i$; (c) slightly less unstable mode for $Re=10^7$ corresponding to the second local peak of the growth rate curves: $k_x=1.80$, $k_y=17.56$, $\omega=0.928+0.0209i$. Thick solid lines, solid lines and dashed lines represent absolute value, real part and imaginary part, respectively.

(see figure 7*c*). It should be noted that the mode associated with the first peak is still unstable for $Re=10^7$, and its pressure eigenfunction is the same as for $Re=10^4$, as seen in figure 11*c*).

In figure 12, we have considered a strongly stratified case ($F=0.5$). Figure 12*(a,b)* shows the pressure eigenfunction of the most unstable radiative mode for two different Reynolds numbers. By comparing these two figures, we observe that the impact of the Reynolds number is much weaker than for the weakly stratified case, as the pressure eigenfunction is almost not modified. Besides, this eigenfunction is very similar to the eigenfunction of the most unstable mode obtained for $Re=10^4$ and $F=3$. However, it is very different from the most unstable inviscid eigenfunction obtained by Candelier *et al.* (2012) for small Froude numbers. The inviscid mode exhibits an oscillating structure which is not present in the viscous mode for $Re=10^4$ and $Re=10^7$ (see figure 12*a,b*). This difference is mainly due to a property already mentioned above: the viscous mode is associated with the first peak and has a small streamwise wavenumber (as for the modes shown in figure 11*a,c*). We suspect that this peak could be of viscous nature. It indeed gives a mode with a non-oscillating structure which resembles that of 2-D TS waves (see figure 5). If we consider the mode associated with the second peak, we obtain an eigenfunction with an oscillatory tail (figure 12*c*) which resembles the inviscid eigenfunction obtained for small Froude numbers (see Candelier *et al.* (2012, figure 4)). It is important to stress that this mode has almost the same growth rate as the most unstable mode.

3.3. Competition between radiative instability and viscous instability

As shown above, the viscous instability is present as soon as $Re > 3981$ for any Froude number, while the radiative instability is active in a domain of the (Re, F) plane which has been displayed in figure 10*(a)*. Both instabilities are then expected to be in competition in a large domain of the parameter space. In figure 13, we have provided a summary of this competition by indicating 5 different domains corresponding to a domain of no instability, 2 domains where there is a single instability active, 2 other domains where one instability dominates the other. This figure clearly demonstrates that the radiative instability is the dominant instability in a large domain of the parameter space. It is the first instability to appear as the

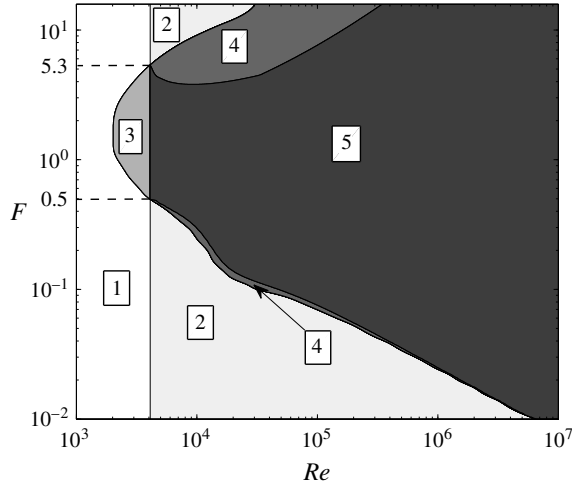


FIGURE 13. Domains of instability in the (Re, F) plane. (1) No instability; (2) viscous instability without radiative instability; (3) radiative instability without viscous instability; (4) both instabilities present but viscous instability dominates radiative instability; (5) both instabilities present but radiative instability dominates viscous instability.

Reynolds number increases in the range $0.5 < F < 5.3$. For $Re = 10^6$, it dominates the viscous instability in the large range $0.03 < F < 30$.

4. Discussion

In this article, we have demonstrated that a stably stratified boundary layer flow on a vertical wall is affected by two instabilities: a classical 2-D viscous instability and a 3-D non-viscous radiative instability. We have shown that the radiative instability is the first instability to appear as the Reynolds number increases for $0.5 < F < 5.3$, and is the dominant instability in a large Froude number interval around $F = 1$ for large Reynolds numbers. In the domain of parameters where the instability growth rate is the largest (large Reynolds numbers, small Froude numbers), the instability is characterized by a streamwise wavelength scaling with the boundary layer thickness and a small transverse wavelength proportional to F . The radiative instability is oscillatory with a frequency close to 1 (that is U/L in dimensional form). The most unstable mode extends up to a few boundary layer thickness.

The work has focused on the temporal stability property of a local boundary layer profile. We have found that the streamwise wavenumber of the most unstable radiative mode increases with the Reynolds number and remains always larger than 0.1 for $F < 16$. For TS waves, we have obtained that the streamwise wavenumber weakly decreases with the Reynolds number but is still larger than 0.05 for $Re = 10^7$. For both types of modes, there is then a clear separation of scales between the instability wavelength and the $O(Re)$ spatial evolution length of the boundary layer flow. This justifies *a posteriori* the local parallel-flow assumption that we have made in neglecting the spatial development of the flow. Nevertheless, it would be interesting to perform a spatial stability analysis (in which the frequency is fixed, and one of the wavenumbers unknown) to gain information on the spatial development of the instability from a localized excitation, as done in Wu & Zhang (2008b).

It may be useful to apply the present results to experimental facilities such as the large stratified water flume of CNRM at Toulouse (Paci *et al.* 2011) to determine whether the radiative instability could develop on the side wall. Toulouse facility is 30 m long and 1.6 m deep. In normal conditions of use, it typically generates on the side walls a boundary layer flow of characteristics $U = 0.1 \text{ m s}^{-1}$, $L = 10 \text{ cm}$ and $N = 1 \text{ rad s}^{-1}$ which gives $Re = 10\,000$ and $F = 1$. The most unstable mode of such a flow has the characteristics $k_x = 0.83$, $k_y = 5.47$, $\omega = 0.7 + 0.012i$. It gives a period $T = 2\pi L / (U \text{Re}(\omega)) \approx 9 \text{ s}$, a growth time $\tau = L / (U \text{Im}(\omega)) \approx 80 \text{ s}$, a streamwise wavelength 75 cm and a transverse wavelength 12 cm. Such a perturbation clearly fits within the channel. It is much stronger than the viscous instability of the boundary layer which has a growth time ten times larger for this Reynolds number. We believe that this instability could be present on the side wall of the channel. We suspect that it could affect the quality of the flow within the channel.

The radiative instability could also be present in real geophysical flows. Consider a stably stratified nocturnal atmospheric boundary layer, as reported in Frehlich, Meillier & Jensen (2008). The velocity and thickness of this boundary layer flow is $U = 10 \text{ m s}^{-1}$ and $L = 100 \text{ m}$, respectively. The buoyancy frequency associated with the stratification is approximately $N = 0.031 \text{ rad s}^{-1}$ while the kinematic viscosity is $\nu = 10^{-5} \text{ m}^2 \text{ s}^{-1}$. This gives $F = 3.2$ and $Re = 10^8$. If such a flow was present on a vertical cliff, it would be unstable with respect to a radiative instability by a mode of characteristics $k_x = 0.95$, $k_y = 13.84$, $\omega = 0.27 + 0.0083i$. This would give a perturbation period $T \approx 3.5 \text{ mn}$ and a characteristic growth time $\tau \approx 20 \text{ mn}$. The streamwise and transverse wavelengths of this perturbation would be 660 m and 45 m, respectively.

The deep ocean is stably stratified. If we assume a buoyancy frequency approximately equal to 0.01 rad s^{-1} (Alford & Gregg 2006) and a kinematic viscosity $\nu = 10^{-6} \text{ m}^2 \text{ s}^{-1}$, a boundary layer flow of velocity $U = 0.15 \text{ m s}^{-1}$ and thickness $L = 10 \text{ m}$ would correspond to the parameters $Re = 1.5 \times 10^6$ and $F = 0.15$. On a vertical ridge or a very steep slope, such a flow would be unstable with respect to the radiative instability by a mode of characteristics $k_x = 1.23$, $k_y = 33$, $\omega = 1 + 0.02i$. This would give a period $T \approx 7 \text{ mn}$, a growth time $\tau \approx 1 \text{ h}$, and a spatial structure of wavelength 51 m in the streamwise direction and 1.9 m in the transverse direction.

We have analysed the stability of a boundary layer flow on a vertical wall. For oceanic applications, it would be more relevant to consider inclined slopes. In that case, the radiative instability is still present but with a weaker growth rate (Candelier *et al.* 2012). However, the radiative instability disappears on a horizontal surface. For the flow on a surface of moderate slope, a stronger competition could exist between viscous and radiative instability, but for large Reynolds numbers, the radiative instability is always expected to dominate as its growth rate does not decrease with the Reynolds number.

Note finally that we have not considered the effect of density diffusion. For both the atmosphere and the ocean, one should consider the temperature diffusion, for which the equivalent Schmidt number (Prandtl number) is of order 1. This stronger diffusion is expected to enhance the damping of the mode but this effect should remain small for the Reynolds numbers relevant to the geophysical applications (typically $Re > 10^6$).

The impact of the radiative instability on the dynamics of the atmosphere or the ocean remains unknown. When it is present, does it only contribute to the local mixing in the boundary layer, or does it induce a mixing further away from the boundary due to the radiative extension of the instability mode are among the interesting questions that have to be addressed. Answering these questions would require an understanding of the nonlinear evolution of the instability. This could constitute a nice objective for the future numerical or experimental works on the subject.

Acknowledgements

This work received support from the French Agence Nationale de la Recherche under the A*MIDEX grant ANR-11-IDEX-0001-02, the LABEX MEC project ANR-11-LABX-0092, the ANR LIPSTIC project ANR-13-JS05-0004-01 and the ANR OLA project ANR-11-BS56-0012. J.C. also acknowledges financial support from China Scholarship Council (CSC 201304490022).

REFERENCES

- ALFORD, M. H. & GREGG, M. C. 2006 Structure, propagation, and mixing of energetic baroclinic tides in Mamala Bay, Oahu, Hawaii. *J. Phys. Oceanogr.* **36**, 997–1018.
- BALMFORTH, N. J. 1999 Shear instability in shallow water. *J. Fluid Mech.* **387**, 97–127.
- BETCHOV, R. & CRIMINALE, W. O. 1967 *Stability of Parallel Flows*. Academic.
- CANDELIER, J., LE DIZÈS, S. & MILLET, C. 2011 Shear instability in a stratified fluid when shear and stratification are not aligned. *J. Fluid Mech.* **685**, 191–201.
- CANDELIER, J., LE DIZÈS, S. & MILLET, C. 2012 Inviscid instability of a stably stratified compressible boundary layer on an inclined surface. *J. Fluid Mech.* **694**, 524–539.
- CHURILOV, S. M. 2005 Stability analysis of stratified shear flows with a monotonic velocity profile without inflection points. *J. Fluid Mech.* **539**, 25–55.
- CHURILOV, S. M. 2008 Stability analysis of stratified shear flows with a monotonic velocity profile without inflection points. Part 2. Continuous density variation. *J. Fluid Mech.* **617**, 301–326.
- DRAZIN, P. G. & REID, W. H. 1981 *Hydrodynamic Stability*. Cambridge University Press.
- FREHLICH, R., MEILLIER, Y. & JENSEN, M. L. 2008 Measurements of boundary layer profiles with in situ sensors and doppler lidar. *J. Atmos. Ocean. Technol.* **25** (8), 1328–1340.
- GRIMSHAW, R. H. J. 1979 On resonant over-reflexion of internal gravity waves from a Helmholtz velocity profile. *J. Fluid Mech.* **90**, 161–178.
- HOWARD, L. N. 1961 Note on a paper of John W. Miles. *J. Fluid Mech.* **10** (04), 509–512.
- KOPEV, V. F. & LEONTEV, E. A. 1983 A coustic instability of a axial vortex. *Sov. Phys. Acoust.* **29**, 111–115.
- LE DIZÈS, S. & BILLANT, P. 2009 Radiative instability in stratified vortices. *Phys. Fluids* **21** (9), 096602.
- LINDZEN, R. S. & BARKER, J. W. 1985 Instability and wave over-reflection in stably stratified shear flow. *J. Fluid Mech.* **151**, 189–217.
- MACK, L. M. 1990 On the inviscid acoustic-mode instability of supersonic shear flows. Part 1: two-dimensional waves. *Theor. Comput. Fluid Dyn.* **2**, 97–123.
- MAHRT, L. 2014 Stably stratified atmospheric boundary layers. *Annu. Rev. Fluid Mech.* **46**, 23–45.
- MCINTYRE, M. E. & WEISSMAN, M. A. 1978 On radiative instabilities and resonant overreflection. *J. Atmos. Sci.* **35**, 1190–1196.
- MILES, J. W. 1961 On the stability of heterogeneous shear flows. *J. Fluid Mech.* **10**, 496–508.
- OHYA, Y. & UCHIDA, T. 2003 Turbulence structure of stable boundary layers with a near-linear temperature profile. *Boundary-Layer Met.* **108**, 19–38.
- PACI, A., KNIGGE, C., ETLING, D., JOHNSON, T., ESLER, G. & CAZIN, S. 2011 Topographic internal waves in the laboratory: two recent experiments carried in the CNRM-GAME stratified water tank. *Geophys. Res. Abstracts* **13**, EGU2011–10299–2.
- PARRAS, L. & LE DIZÈS, S. 2010 Temporal instability modes of supersonic round jets. *J. Fluid Mech.* **662**, 173–196.
- PLOUGONVEN, R. & ZEITLIN, V. 2002 Internal gravity wave emission from a pancake vortex : an example of wave-vortex interaction in strongly stratified flows. *Phys. Fluids* **14**, 1259–1268.
- RIEDINGER, X. & GILBERT, A. D. 2014 Critical layer and radiative instabilities in shallow-water shear flows. *J. Fluid Mech.* **751**, 539–569.
- RIEDINGER, X., LE DIZÈS, S. & MEUNIER, P. 2010 Viscous stability properties of a Lamb–Oseen vortex in a stratified fluid. *J. Fluid Mech.* **645**, 255–278.

- RIEDINGER, X., LE DIZÈS, S. & MEUNIER, P. 2011 Radiative instability of the flow around a rotating cylinder in a stratified fluid. *J. Fluid Mech.* **672**, 130–146.
- SATOMURA, T. 1981 An investigation of shear instability in a shallow water. *J. Met. Soc. Japan* **59** (1), 148–167.
- WU, X. & ZHANG, J. 2008*a* Instability of a stratified boundary layer and its coupling with internal gravity waves. Part 1. Linear and nonlinear instabilities. *J. Fluid Mech.* **595**, 379–408.
- WU, X. & ZHANG, J. 2008*b* Instability of a stratified boundary layer and its coupling with internal gravity waves. Part 2. Coupling with internal gravity waves via topography. *J. Fluid Mech.* **595**, 409–433.